Journal of Applied Physics

RESEARCH ARTICLE | JANUARY 19 2012

Stability and topological transformations of liquid droplets on vapor-liquid-solid nanowires

Edwin J. Schwalbach; Stephen H. Davis; Peter W. Voorhees; James A. Warren; Daniel Wheeler

Check for updates

J. Appl. Phys. 111, 024302 (2012)
https://doi.org/10.1063/1.3676451

View Online
Export Citation

Articles You May Be Interested In

Nonaxisymmetric droplet unpinning in vapor-liquid-solid-grown nanowires

J. Appl. Phys. (September 2013)

Advanced core/multishell germanium/silicon nanowire heterostructures: The Au-diffusion bottleneck

Appl. Phys. Lett. (July 2011)

Temperature dependent resistance and cryogenic microwave spectroscopy of Au decorated silicon nanowires

J. Appl. Phys. (June 2011)

29 September 2025 19:45:15

Nanotechnology & Materials Science
Optics & Photonics
Impedance Analysis
Scanning Probe Microscopy
Sensors
Failure Analysis & Semiconductors

Unlock the Full Spectrum.
From DC to 8.5 GHz.
Your Application. Measured.
Find out more
Zurich Instruments

AIP Publishing

Stability and topological transformations of liquid droplets on vapor-liquid-solid nanowires

Edwin J. Schwalbach,[1,2] Stephen H. Davis,[3] Peter W. Voorhees,[1,3,a)] James A. Warren,[2] and Daniel Wheeler[2]
[1]*Department of Materials Science and Engineering, Northwestern University, Evanston, Illinois 60208, USA*
[2]*Metallurgy Division, Material Measurement Laboratory, National Institute of Standards and Technology, Gaithersburg, Maryland 20899, USA*
[3]*Department of Engineering Sciences and Applied Mathematics, Northwestern University, Evanston, Illinois 60208, USA*

(Received 11 October 2011; accepted 13 December 2011; published online 19 January 2012)

The Vapor-Liquid-Solid method is one of the most popular techniques for growing semiconducting nanowires, and the stability of the liquid droplet is an important factor controlling wire morphology and, ultimately, functionality. Earlier theoretical work on axisymmetric systems indicates that the lowest-energy liquid configuration varies with surface energies, wire radius, and fluid volume. We test these predictions with a fully dynamic phase-field model that incorporates viscous fluid flow. Under conditions predicted by this earlier theoretical work, we observe the pinning of the liquid to the top face of a nanowire, a condition necessary for wire growth. To study the stability of the droplet, we apply perturbations to the liquid shape and find that the system can transition to a metastable configuration, a local minimum in the energy landscape. Furthermore, the transition pathway to this local minimum depends on the magnitude of the perturbations. Under conditions that favor a liquid on the sidewalls of the wire, we observe a spontaneous transition of the liquid from a droplet to an annular configuration through an intermediate state that is not predicted by theory. The time scales and contact-line speeds for these transitions are determined through simulation and are consistent with approximations based on simple dimensional analysis.
© *2012 American Institute of Physics*. [doi:10.1063/1.3676451]

29 September 2025 19:45:15

I. INTRODUCTION

The Vapor-Liquid-Solid (VLS) method has been extensively used to grow defect-free single-crystal semiconducting nanowires. In this technique, a vapor-phase precursor feeds the growth of a filamentary crystal through a liquid alloy droplet.[1] Typically, the liquid droplet remains on the tip of the growing crystal and the growth proceeds along a well-defined crystallographic direction. However, there are many examples, going back to some of the earliest reports of VLS growth,[2] of nanowires which "kink," or change their growth directions. Whereas kinks are often considered to be defects, morphologically complex wires that exhibit controlled kinking or branching are useful for biological probes and photovoltaic applications.[3,4] Many experiments indicate that kinking and branching are sensitive to changes in the vapor-phase atmosphere.[5–12]

The stability of the liquid droplet and the pinning of the vapor-liquid-solid contact line are important factors during wire growth. Roper *et al.*[13] analytically computed the energy of several axisymmetric equilibrium configurations, shown in Fig. 1(a), to determine the lowest-energy state and identify when the "droplet," Fig. 1(a) configuration B, might be unstable as a function of the surface-energy ratios γ_{sv}/γ_{lv} and γ_{sl}/γ_{lv} (where γ_{sv}, γ_{sl}, and γ_{lv} are the solid-vapor, solid-liquid, and liquid-vapor surface energies, respectively) and the size of the solid wire relative to the liquid alloy, characterized by the ratio $R_s/V_l^{1/3}$ (where R_s is the solid radius and V_l is the liquid volume). The droplet form (displayed in Fig. 1(a), configuration B) is observed in experiments during typical nanowire growth, and thus its stability is of great practical importance. Under certain conditions, however, the annular configuration (Fig. 1(a), configuration D) has the lowest energy and a transition of the liquid from the droplet to annular configuration might disrupt nanowire growth or initiate a growth direction change. The analysis of Roper *et al.*[13] is based on energy minimization arguments, and finds that the Young's angle, θ_Y, is an important parameter, where θ_Y is given by

$$\cos\theta_Y = \frac{\gamma_{sv} - \gamma_{sl}}{\gamma_{lv}}. \tag{1}$$

While their work identifies the lowest energy configurations as a function of the surface energies, it does not predict how a transition between configurations might occur.

Schwarz and Tersoff[14,15] have recently simulated nanowire growth in a two-dimensional model. Their model qualitatively reproduces many experimentally observed growth features, including kinking. Specifically, they find that the unpinning of the contact line is one critical step in the kinking process. Their model, however, takes the liquid to be in mechanical equilibrium at all times, and thus it instantaneously relaxes between low energy configurations. It is possible that the pathways by which these transitions occur could influence the droplet topology, and, therefore, wire morphology. In order to study such topological transitions, a fully dynamic model is necessary.

a)Electronic mail: p-voorhees@northwestern.edu.

 © 2012 American Institute of Physics

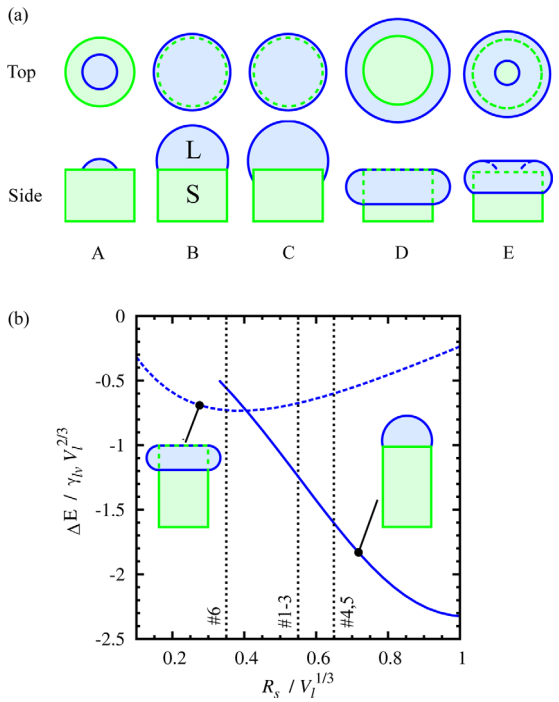

FIG. 1. (Color online) (a) Top and side views of axisymmetric liquid configurations investigated by Roper *et al.*[13] with liquid and solid labeled L (blue) and S (green), respectively. Configurations B and D will be referred to as the "droplet" and "annular" configurations, respectively. (b) The normalized total energy for the annular and droplet configurations for a system with $\theta_Y = 55°$. The annular configuration (dashed) has a lower energy when $R_s/V_l^{1/3} < 0.4$, and the droplet configuration (solid) is energetically favorable for $R_s/V_l^{1/3} > 0.4$. Dotted vertical lines indicate the value of $R_s/V_l^{1/3}$ for specific simulation numbers. Adapted from Ref. 13.

The phase-field method[16] has previously been used to study liquid droplets and contact-line motion.[5,17–22] The technique can handle fully dynamic models including both convective and diffusive mass transport, which are important in unpinned contact-line motion and crystal growth. The technique also handles surface-energy effects (capillarity), which have been identified as important factors in droplet stability in theoretical work.[13] Finally, phase-field modeling is a diffuse-interface method and can easily handle topological transitions such as contact-line formation and coalescence. In earlier work,[5] we employed a phase-field model to investigate how liquid droplets dewet substrates during the early stages of Au catalyzed Si VLS growth, as well as the kinetics of unpinned contact-line motion. Here, we use the same model, but instead focus on the stability of and topological transitions between different liquid configurations with implications for nanowire morphology. These simulations show that transitions between different droplet configurations are indeed dynamically possible, and indicate the experimental importance of control over liquid droplet volume and surface energies.

To examine the relevant timescales for VLS growth before introducing the phase-field model in the next section, it is useful to review timescales associated with the simpler system of a droplet spreading on a planar, inert substrate. Typically, such a droplet will undergo two spreading stages. The initial stage is inertial in nature and is characterized by rapid changes in spreading rate and contact-line oscillations in position and/or velocity. The spreading then transitions to a viscous stage characterized by a relatively steady spreading rate and constant radius of curvature. Other stages of spreading may also occur if the substrate is assumed to be reactive.

An analysis by Schiaffino and Sonin[23] that estimates the period t_i for oscillations of the droplet during the early inertial regime is

$$t_i = \sqrt{\frac{\rho_l R_0^3}{\gamma_{lv}}}, \tag{2}$$

and the corresponding characteristic contact-line speed is

$$v_i = \sqrt{\frac{\gamma_{lv}}{\rho_l R_0}}, \tag{3}$$

where ρ_l is the liquid density, and R_0 is the droplet radius. The dissipation time, t_d, over which these oscillations are damped by viscosity is given by

$$t_d = \frac{\rho_l R_0^2}{\eta_l}, \tag{4}$$

where η_l is the dynamic viscosity of the liquid. We note that the dimensionless ratio t_i/t_d is equal to the Ohnesorge number,[23]

$$\mathrm{Oh} = \frac{\eta_l}{\sqrt{\rho_l R_0 \gamma_{lv}}}. \tag{5}$$

During the later stages of spreading, the liquid-vapor interface is characterized by an average radius of curvature R_0 with small variations ΔR. When ΔR is sufficiently small compared to R_0, these variations lead to capillary pressure differences ΔP, estimated by

$$\Delta P = \frac{\gamma_{lv}}{R_0}\frac{\Delta R}{R_0}, \tag{6}$$

which drive fluid flow. This flow is resisted by viscous forces, and, by modifying the analysis of Schiaffino and Sonin to account for the driving force ΔP, the time scale t_v for this flow is found

$$t_v = 100\frac{\eta_l R_0^2}{\gamma_{lv}\Delta R}, \tag{7}$$

and the characteristic speed is

$$v_v = \frac{\gamma_{lv}\Delta R}{100\eta_l R_0}. \tag{8}$$

Schiaffino and Sonin's result is recovered in the limit $\Delta R/R_0 \to 1$. The numeric prefactors in Eqs. 7 and 8 account for empirical observations which indicate that the transition from inertial to viscous dominated resistance occurs around $\mathrm{Oh} = 10^{-2}$ rather than $\mathrm{Oh} = 1$.[23]

Table I gives estimates for the inertial and viscous time and speed scales using physical and geometric properties characteristic of the Au-Si nanowire system according to

29 September 2025 19:45:15

TABLE I. Time and contact-line speed estimates for various physical regimes according to an analysis by Schiaffino and Sonin.[23] Physical parameters are typical of a Au-Si nanowire: $\eta_l = 5 \times 10^{-3}$Pa s, $\gamma_{lv} = 1\text{Jm}^{-2}$, $\rho_l = 13625\text{kg m}^{-3}$, $R_0 = 40\text{nm}$, $\Delta R/R_0 = 0.05$.

Regime	Time Scale [ns]	Speed [m s^{-1}]
Inertial oscillations, t_i, v_i	0.93	43
Dissipation time, t_d	4.4	–
Viscous spreading, t_v, v_v	400	0.10

Eqs. 2–4,7,8. Also, according to Eq. 5, Oh ≈ 0.2 for this system, which indicates that inertia will play a role during only the earliest stages of the temporal evolution of the fluid, whereas capillarity and viscosity will dominate the later stages. The short time scales and large velocities are a result of the small radii of curvature and hence large pressures in the liquid; surface tension is an important factor in this nanoscale fluid-flow problem.

II. MODEL

A bulk free-energy function sets the equilibrium densities and compositions of the phases. In this work, the Au-Si alloy is modeled as an ideal solution of two pure materials, A and B, which have the same molar mass m. Each of the pure materials has a free energy which is the sum of a solid and fluid phase, the latter of which is a van der Waals fluid that separates into low and high density states below a critical temperature. This model has been used by Wheeler *et al.*[22] to simulate reactive wetting of micrometer diameter liquid droplets on planar substrates.

The molar Helmholtz free energy F_m is

$$F_m(X, V_m, \phi) = XF_A(V_m, \phi) + (1-X)F_B(V_m, \phi) + RT[X\ln(X) + (1-X)\ln(1-X)], \quad (9)$$

where X is the mole fraction of component A, V_m is the molar volume, ϕ is an order parameter, and F_i is the molar free energy of pure component i. The energies of the pure components are

$$F_i(V_m, \phi) = p(\phi)F_i^s(V_m) + [1-p(\phi)]F_i^{vw}(V_m) + \phi^2(1-\phi)^2 W, \quad (10)$$

where F_i^s and F_i^{vw} are the free energy of solid and van der Waals fluid of component i, respectively, and W is an energy barrier. The order parameter ϕ takes on a value of 1 in the solid phase and 0 in the fluid, and an interpolation function $p(\phi)$ blends the two energies,

$$p(\phi) = \phi^3(6\phi^2 - 15\phi + 10). \quad (11)$$

The pure solid has a molar free energy,

$$F_i^s(V_m) = A_i + B\left(\frac{V_m}{V_0^s} - 1\right)^2, \quad (12)$$

where A_i, B, V_0^s are constants. The equilibrium molar volume of the solid is V_0^s in the limit of zero pressure and the bulk modulus $K \approx 2B/V_0^s$.

TABLE II. Values of Si mole fraction and total density for solid, liquid, and vapor phases to approximate the experimentally relevant Au-Si system assuming a constant molar mass $m = 0.1547$[kg/mol].

Phase	X_{Si}	ρ [kg m^{-3}]	$V_m = m/\rho$ [m^{3}mol^{-1}]
Solid	0.90	13625	1.135×10^{-5}
Liquid	0.25	13625	1.135×10^{-5}
Vapor	0.90	136.25	1.135×10^{-3}

The fluid phases are modeled as a van der Waals fluid with a free energy F_i^{vw},

$$F_i^{vw}(V_m) = -\frac{e_i}{V_m} - RT\ln(V_m - V_{0i}^{vw}). \quad (13)$$

In order to model the Au-Si system,[24] we take the values of density (and thus molar volume) and mole fraction listed in Table II. The constant molar mass m and density of the liquid are determined with Vegard's law for a liquid that has an Au mole fraction $X_{Au} = 0.75$ is set equal to that of the liquid, and the vapor density is set 100× lower than ρ_l. The values of ρ_s and ρ_v do not strongly affect the liquid flow field, and these choices are computationally convenient. The resulting bulk properties are summarized in Table III, and will be used for the remainder of this work. This free-energy yields a system with a large change in ϕ across the solid-fluid phases, and a large change in ρ between the vapor and condensed (liquid and solid) phases.

To incorporate the effects of surface energy, gradient-energy terms are added to the bulk free-energy function to create a free-energy functional $\mathcal{F}$. The model used here is based on the work of Sekerka and Bi.[25,26] The free-energy functional is

$$\mathcal{F} = \int_{\mathcal{V}} F_V(\rho_A, \rho_A, \phi) + \left[\frac{\kappa_\rho}{2}\left(|\nabla\rho_A|^2 + |\nabla\rho_B|^2\right) + \frac{\kappa_\phi}{2}|\nabla\phi|^2\right] d\mathcal{V}, \quad (14)$$

where $F_V = F_m/V_m = F_m\rho/m$ is the free energy per unit volume computed from Eq. (9) and κ_ρ and κ_ϕ are the

TABLE III. Model parameters. For some simulations, κ_φ and W are modified from the values listed here. See Table V.

Parameter	Value	SI Units
T	650	K
m	0.1547	kg mol^{-1}
A_{Si}	41603	J mol^{-1}
A_{Au}	41423	J mol^{-1}
e_{Si}	0.26560	J m^3 mol^{-2}
e_{Si}	0.46987	J m^3 mol^{-2}
V_0^{vw}	9.6930×10^{-6}	m^3 mol^{-1}
V_0^s	1.1356×10^{-5}	m^3 mol^{-1}
B	2×10^5	J mol^{-1}
κ_ρ	3.25×10^{-17}	J m^5 kg^{-2}
κ_φ	9.75×10^{-10}	J m^{-1}
W	10^4	J mol^{-1}

29 September 2025 19:45:15

gradient-energy coefficients on the density and order-parameter gradients, respectively. Using a standard variational approach described in Ref. 25, it is straightforward to show that a nonclassical chemical potential μ_i^{NC} is

$$\mu_i^{NC} = \frac{\rho}{m}\frac{\partial F_m}{\partial \rho_i} - \kappa_\rho \nabla^2 \rho_i. \tag{15}$$

Similarly, the phase potential Φ is

$$\Phi = -\frac{\rho}{m}\frac{\partial F_m}{\partial \phi} + \kappa_\phi \nabla^2 \phi. \tag{16}$$

Time evolution of this system is governed by mass and momentum balances as well as non-conserved Allen-Cahn dynamics for the order parameter. For convective and diffusive mass transport, the mass balance of component i is

$$\frac{\partial \rho_i}{\partial t} = -\nabla \cdot (\rho_i \vec{v}) - \nabla \cdot \vec{j}_i, \quad i = \mathrm{A}, \mathrm{B}, \tag{17}$$

where ρ_i is the local mass density of component i, $\vec{v}$ is the convective velocity vector, and $\vec{j}_i$ is the diffusive mass flux. The diffusive mass flux is proportional to gradients of the non-classical chemical potential difference,

$$\vec{j}_{\mathrm{A}} = -M\nabla\left(\mu_{\mathrm{A}}^{\mathrm{NC}} - \mu_{\mathrm{B}}^{\mathrm{NC}}\right), \tag{18}$$

$$\vec{j}_{\mathrm{B}} = -\vec{j}_{\mathrm{A}}, \tag{19}$$

where M is the mass mobility which is related to the diffusion coefficient D discussed in Ref. 22. The full form of the order-parameter dependent mass mobility is

$$M = M_s^{\phi^4} M_f^{1-\phi^4} X(1-X), \tag{20}$$

where M_s is the mobility of the solid phase and M_f is the mobility in the fluid phases. These quantities are set such that $D_l = 4 \times 10^{-10}\mathrm{m}^2\mathrm{s}^{-1}$ and $D_s = 4 \times 10^{-14}\mathrm{m}^2\mathrm{s}^{-1}$.

In this model, all three phases are treated as fluids and are subject to the momentum balance expressed by the Navier-Stokes equations,

$$\frac{\partial \vec{v}}{\partial t} = -\vec{v} \cdot \nabla \vec{v} + \frac{1}{\rho}\nabla \cdot \boldsymbol{\sigma}, \tag{21}$$

where the divergence of the stress tensor $\nabla \cdot \boldsymbol{\sigma}$ can be simplified to

$$\nabla \cdot \boldsymbol{\sigma} = 2\nabla \cdot (\eta \boldsymbol{D}) + \rho_{\mathrm{A}} \nabla \mu_{\mathrm{A}}^{\mathrm{NC}} + \rho_{\mathrm{B}} \nabla \mu_{\mathrm{B}}^{\mathrm{NC}} - \Phi \nabla \phi. \tag{22}$$

Here, η is the dynamic viscosity, and $\boldsymbol{D}$ is the rate of deformation tensor,

$$\boldsymbol{D} = \frac{1}{2}\left[\nabla \vec{v} + (\nabla \vec{v})^{\mathrm{T}}\right]. \tag{23}$$

The terms with $\nabla \mu_i^{\mathrm{NC}}$ and $\nabla \phi$ in Eq. (22) incorporate both the classical pressure gradient through the $\partial F_m / \partial \rho_i$ terms in μ^{NC}, as well as additional terms that give rise to stresses due to interfacial effects. These governing equations are solved on an axisymmetric cylindrical coordinate system using FiPy,[27] a numerical partial differential equation solving tool developed at the NIST Center for Theoretical and Computational Materials Science.

TABLE IV. Bulk-phase kinetic parameters.

Parameter	Solid	Fluid	Vapor	SI Unit
Viscosity η	5×10^{3}	5×10^{-3}	5×10^{-3}	Pa s
Diffusivity D	4×10^{-14}	4×10^{-10}	4×10^{-8}	$\mathrm{m}^2\ \mathrm{s}^{-1}$
φ mobility M_φ	15.4	15.4	15.4	$\mathrm{m}^3\mathrm{J}^{-1}\ \mathrm{s}^{-1}$

Whereas the constitutive equation of all phases is that of a Newtonian fluid, convective flow in the solid ($\phi = 1$) is prevented by using an appropriate order-parameter dependent function for the viscosity,

$$\eta = \eta_s^{\phi^4} \eta_l^{1-\phi^4}. \tag{24}$$

The liquid and vapor fluids are assumed to have the same viscosity, $\eta_l = 5 \times 10^{-3}$ Pa s,[28] and the viscosity in the solid phase, η_s, is larger by a factor of 10^6. The value of η_s is large enough to prevent an unphysical convective motion in the solid phase during the time scales explored in these simulations.

Finally, the nonconserved order parameter evolves according to an Allen-Cahn equation with a convective term,

$$\frac{\partial \phi}{\partial t} = -\vec{v} \cdot \nabla \phi + M_\varphi \Phi, \tag{25}$$

where M_ϕ is the mobility of the order-parameter field which is taken to be spatially uniform. The value of M_ϕ is chosen to be fast enough such that relaxation occurs at time scales much faster than the phenomena explored here. In simple one-dimensional growth simulations, the growth speed is not affected until M_ϕ is reduced by 3–4 orders of magnitude compared to the value used in these simulations. For some calculations described in the following chapter, $M_\phi = 0$ is used to fix the shape of the solid in order to study contact-line motion on time scales where crystal growth is negligible. Table IV gives a summary of all of the bulk-phase kinetic parameters.

III. RESULTS

Phase-field simulations are performed to test the theoretical predictions of Ref. 13 as well as to determine the topological pathways between different liquid states. In Sec. III A, we show that the liquid is, indeed, pinned to the top of a wire under suitable surface energy ratios and $R_s/V_l^{1/3}$ as predicted by Roper *et al.*[13] Then, in Sec. III B, a system which favors the droplet configuration undergoes a transformation into a metastable liquid configuration when a suitable perturbation is applied to the liquid shape. Finally, in Sec. III C, a system which favors the annular configuration (D in Fig. 1(a)), undergoes a spontaneous transformation from a droplet to an annular liquid through an intermediate topology. These results confirm the predictions of Ref. 13, but also indicate that the liquid can exist in metastable configurations, and show that complex liquid configurations are possible during

29 September 2025 19:45:15

TABLE V. Model parameters and nominal equilibrium values of the surface-energy ratios and Young's angle θ_Y used to test the droplet pinning predictions from Ref. 13.

Sim.	κ_φ $[\mathrm{Jm}^{-1}]$	W $[\mathrm{Jmol}^{-1}]$	γ_{lv} $[\mathrm{Jm}^{-2}]$	γ_{sv}/γ_{lv}	γ_{sl}/γ_{lv}	θ_Y [deg]
#1	9.75×10^{-11}	10^4	0.980	1.22	0.650	55
#2	9.75×10^{-10}	10^5	0.980	1.50	0.866	51

transformations between favored states. Nanowire morphology depends on the liquid configuration during growth, and thus these simulations give insights into conditions that favor branching and kinking during growth. All simulations are performed in axisymmetrical cylindrical coordinate systems.

A. Pinning

First, we consider two systems using the parameters listed for Simulations #1 and #2 in Table V. With these parameters, the droplet configuration has the lowest total energy when $R_s/V_l^{1/3}>0.4$ as shown in Fig. 1(b). Simulations #1–2 are carried out with $R_s = 35\mathrm{nm}$ and a liquid volume that gives $R_s/V_l^{1/3} = 0.55$, and thus the droplet configuration is the lowest energy state according to Fig. 1(b).

The initial condition is chosen such that the liquid covers only the top face of a solid cylindrical wire. The initial liquid-vapor interface is spherical except within approximately two interface thicknesses of the contact line. This local disturbance provides a weak perturbation to test the stability of the pinned droplet configuration. The order parameter is allowed to vary over a (short) equilibration period of 1 ns in order to attain the appropriate interface profiles and therefore surface energies. Because this model has isotropic surface energies, the melting process tends to round the solid corner. In order to maintain the appropriate solid wire shape, the order parameter mobility M_ϕ is reduced to zero after the equilibration period. After initial oscillations in contact-line position with amplitude on the order of the interface thickness, the system settles to a state with the contact line pinned at the corner of the solid wire with a contact angle in the range $\theta_Y \leq \theta \leq \theta_Y + \pi/2$, as expected.[29] Contact angles are measured using the methodology outlined in Ref. 20.

This set of simulations indicates that the droplet is, indeed, a stable configuration in this range as predicted by energy arguments given in Ref. 13; normal VLS wire growth is expected under these conditions. The perturbations to the droplet configurations in this section are relatively weak, and responses of the system to much larger perturbations are explored in the next section.

B. Forced droplet to annulus transformation

A series of simulations using initial conditions with an intermediate configuration, shown in Fig. 2, are performed to investigate the stability of the droplet configuration to large perturbations. This initial condition is similar to configuration E in Fig. 1(a) and has two contact lines, one on the top face, and a second on the sidewall. In the simulations described in this section, #3–5, the surface-energy ratios and

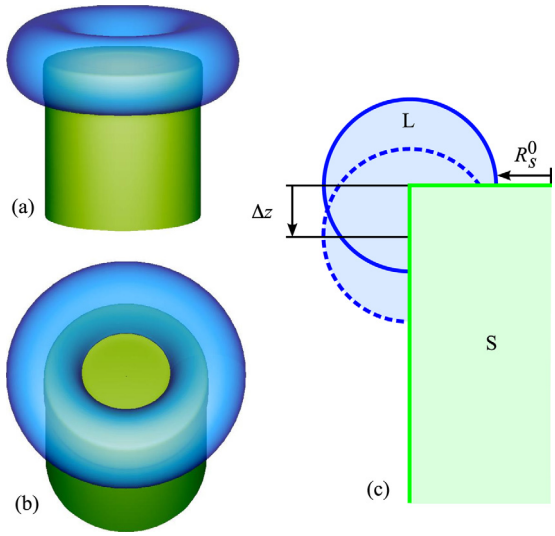

FIG. 2. (Color online) (a) Side and (b) top views of the initial condition used to investigate droplet stability. (c) A schematic cross section showing the radius of the top contact line R_s^0 and the vertical shift of Δz. The solid wire is labeled S (green) and the liquid L (blue).

$R_s/V_l^{1/3}$ are such that the droplet configuration is the global energy minimum, as indicated in Fig. 1(b). Whereas the droplet is favored in this region of the parameter space, the analysis of Roper *et al.*[13] indicates that the annular configuration is still a *local* energy minimum under these conditions. This simulation will allow us to determine if this metastable state is accessible under these conditions.

Figure 2 shows side (a) and top (b) views of an initial configuration where the liquid phase covers part of both the top face and the wire sidewall. A detailed cross section of this configuration is shown in Fig. 2(c). The first liquid configuration, drawn with a solid line, consists of a circular liquid element centered on the solid corner. This configuration is defined to have a vertical shift, $\Delta z = 0$, and the radius of the contact line on the top face is R_s^0. The second liquid configuration, drawn with a dashed liquid-vapor interface, has a downward vertical shift, $\Delta z > 0$, and consequently a larger value of R_s^0. Note that this configuration also has a smaller liquid volume than for $\Delta z = 0$, and therefore a larger value of $R_s/V_l^{1/3}$. According to Ref. 13 and Fig. 1(b), an increase in $R_s/V_l^{1/3}$ tends to increase the stability of the droplet configuration with respect to the annular configuration.

In Simulation #3, shown in Fig. 3, $\Delta z = 0$ and the starting contact angle of both contact lines is 90°. The contact line on the top face of the solid immediately begins moving toward the center of the droplet, visible in Figs. 3(a) and 3(b) and in the streamlines of the flow field in Fig. 4. The contact line on the sidewall moves downward during this time period in order to reduce the contact angle from 90° toward $\theta_Y \approx 50°$, also visible in Fig. 4.

As the contact line on the top face moves toward the center of the wire, the curvature of the liquid-vapor interface becomes increasingly negative. This leads to rapid contact-line motion approaching $80\,\mathrm{m\ s}^{-1}$consistent with the estimate in Table I and a complete closing of the hole on the top face of the wire in little more than 1 ns. The motion is so

29 September 2025 19:45:15

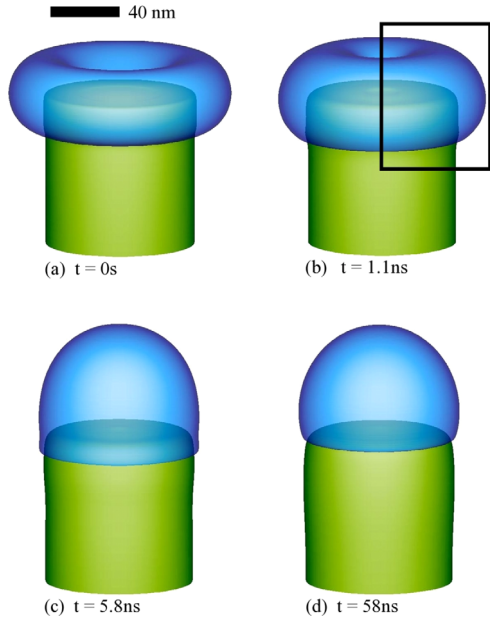

FIG. 3. (Color online) Evolution of Simulation #3 showing the rapid closing of the initial hole on the top face, (a)–(c), and the eventual settling into the droplet configuration in (d). The convective flux in the boxed portion of (b) is shown in detail in Fig. 4.

rapid and the contact line is sufficiently far from its equilibrium profile that it is difficult to unambiguously locate the contact line, and thus a definitive contact-line speed is not reported. The initial downward motion of the contact line on the sidewall is weak compared to the contact-line motion driven by curvature on the top face, and is arrested in 2 ns. The flow near the bottom contact line then reverses and all of the liquid is drawn to the top face with the contact line eventually pinning near the solid corner. After several small oscillations with a period consistent with Eq. (2), the droplet approaches its equilibrium pinned configuration, visible in Fig. 3(c), in less than 10 ns, consistent with the dimensional analysis estimate of dissipation-time in Table I. The contact line and flow field are completely quiescent after roughly 60 ns, Fig. 3(d).

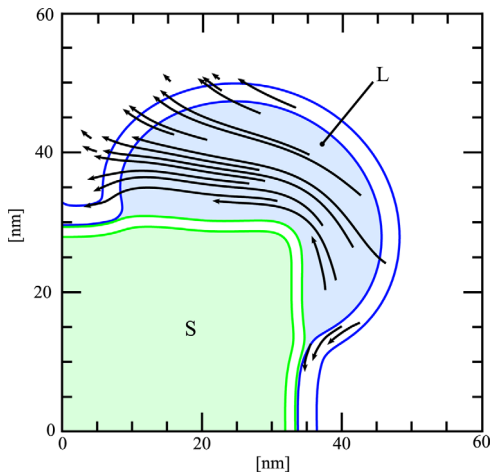

FIG. 4. (Color online) Cross section from Simulation # 3, (boxed region in Fig. 3(b), $t = 1.1$ns), with streamlines of the $\rho\vec{v}$ field. Parallel lines indicate diffuse interface regions. Strong convective flux is closing the hole on the top face, however there is a weak downward flux at the contact line on the sidewall.

Figure 4 shows streamlines of the convective mass flux $\rho\vec{v}$ for the boxed region of Fig. 3. The strong curvature driven flow which closes the hole on the top face of the droplet is clearly visible. There is also a weak flow near the bottom contact line driven by the nonequilibrium sidewall contact angle of the initial condition. This flow is eventually overwhelmed by the upward flow. Streamlines end near the liquid-vapor interface because of the 100 fold decrease in ρ between these two phases. Additionally, there is no convective flux in the solid phase because of the high viscosity and short time scale.

In Simulation #4 shown in Fig. 5, the initial liquid-phase is translated downward by a distance $\Delta z = 0.258\ R_s$, decreasing the contact angle on the top face as well as increasing the radius of the top contact line compared to the value in the previous simulation, seen in Fig. 5(a). The contact angle on the sidewall still has an initial value of 90°.

The initial motion of the top contact line is still toward the center of the top face, and the side contact line moves down the sidewall as seen in Figs. 5(a) and 5(b). The top contact line does not spread as quickly as in the previous simulation due to the reduced curvature of the liquid-vapor interface; instead, its speed is much closer to that of the downward speed of the sidewall contact line. The liquid-vapor interface deforms near the solid corner, Fig. 5(c), and eventually the liquid pinches into two volumes roughly 50 ns after the simulation starts. This topological change leaves a liquid ring with thickness on the order of that of the interface wetting the top face and another liquid volume wetting the sidewall, Fig. 5(d). The liquid ring on the top face eventually

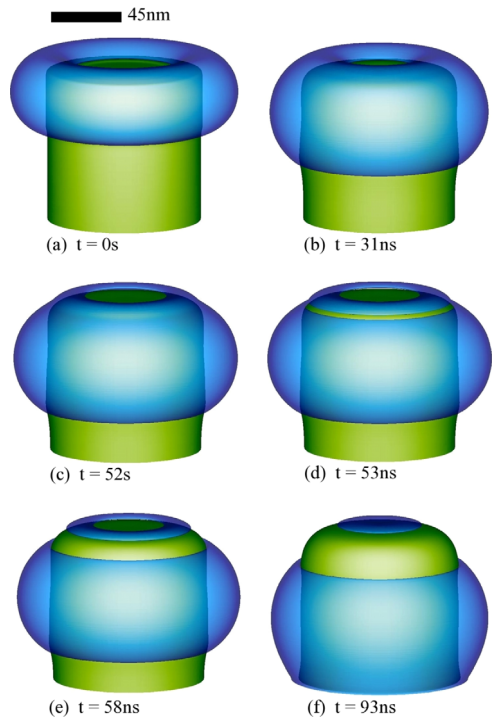

FIG. 5. (Color online) Evolution of Simulation #4 with liquid translated downward. The liquid pinches, (c)-(d), and wets both the top and sidewalls of the wire.

29 September 2025 19:45:15

closes, and forms a liquid layer, Fig. 5(f). It is likely that coarsening of the liquid on the top face of the wire would lead to a configuration with liquid wetting only the sidewalls, as was observed for a similar topology induced by anisotropic crystal growth in earlier studies.[5] However, the liquid wetting the sidewall eventually touches the bottom of the simulation domain seen in Fig. 5(f), at which point the simulation is stopped.

In the final simulation in this series, Simulation #5 shown in Fig. 6, the initial liquid is translated downwards by a distance $\Delta z = 0.33\ R_s$, even further downwards than in the previous calculation. The top contact line moves off of the top face onto the sidewall and there is no significant pinching of the liquid-vapor interfaces as in Simulation #4. The total elapsed time for the droplet to come to rest wetting only the sidewall of the nanowire is approximately 90 ns, quite similar to that observed for the transition in Simulation #4. Recall that the lowest energy state is a droplet wetting the top face only for Simulations #3–5, and thus the final state observed for Simulations #4–5 is not a global equilibrium configuration, but rather a local minimum.

Several other simulations with initial translations in the range $0 < \Delta z \leq 0.256\ R_s$ all transition to the droplet configuration. A critical value that determines the final configuration is then $\Delta z_{\text{crit}} = 0.257\ R_s$ for this particular class of initial geometry and perturbation; translations below this value result in droplets, and above this value the liquid moves down the sidewall of the nanowire. While this value of Δz_{crit} is specific to these simulations, the behavior of a "critical perturbation" necessary to transition to the annular configuration is likely general.

This series of simulations shows that it is possible for the liquid phase to exist in a metastable configuration rather than simply the global energy minimum. With a large enough perturbation, the annular configuration, which is a local minimum in energy for the particular values of $\gamma_{sv}, \gamma_{sl}, \gamma_{lv}$ and $R_s/V_l^{1/3}$ employed in Simulations #3–5, is an accessible state. Additionally, the result in Fig. 5 shows that transient intermediate states, not predicted by the energy minimization technique, are possible. This indicates that the transition *pathway* is important and difficult to predict using simple arguments. Also, the pinching of the liquid-vapor interface and coalescence of contact lines observed in Fig. 5 is a topological change that is difficult to handle with front-tracking or sharp-interface methods, whereas they offer no particular challenge for the phase-field technique. Finally, liquid on the sidewalls of a growing wire could introduce branches thus having important consequences for wire morphology.

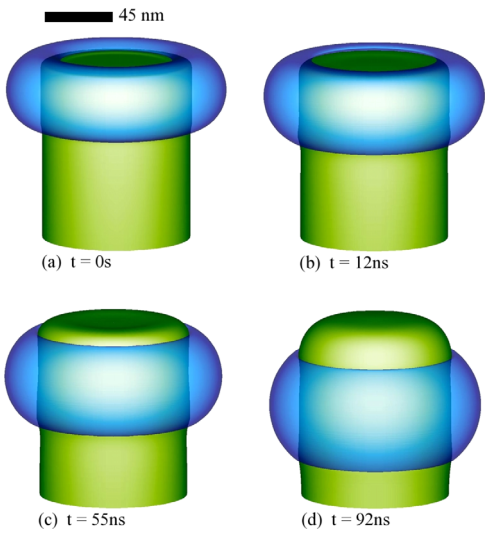

FIG. 6. (Color online) Evolution of Simulation #5 showing rapid dewetting of the top surface without pinching of the liquid droplet.

When the droplet configuration is energetically favored, the initial configuration necessary to achieve a final annular state requires a global change in the liquid topology compared to the low-energy droplet. A second contact line develops on the top face and much of the initial liquid has to wet the sidewall. Such a dramatic change in topology may or may not arise spontaneously in the lab. These calculations, therefore, indicate that the energy barrier between the droplet and annular configuration is significant when the droplet is the favored state. Thus, for the parameters used in this section the droplet is not only an equilibrium configuration as predicted in Fig. 1(b), but a very stable one within the constraint of allowing only axisymmetric perturbations.

C. Topological transition of an unstable droplet

For the surface-energy ratios listed for Simulation #2 in Table V, the annular configuration is favored for $R_s/V_l^{1/3} < 0.4$. In this section, an initial droplet configuration, shown in Fig. 7(a), is employed for Simulation #6. The wire radius is reduced to 22 nm and the liquid volume is such that $R_s/V_l^{1/3} = 0.35$ making the annular configuration energetically favored, shown in Fig. 1(b). The initial contact angle is 140°, close to the limit $\theta_Y + 90°$. Again, the initial liquid-vapor interface is spherical except to within 2–3 interface thicknesses of the contact line, providing a weak initial perturbation to the droplet shape.

The contact line, which starts out just above the solid corner in Fig. 7(a), rapidly moves around the corner and onto the sidewall. This transition occurs between Figs. 7(a) and 7(b) and takes about 1 ns, with the contact-line speed peaking just above 1 m s^{-1} The contact line continues moving down the sidewall of the wire; however, this motion disturbs the initial spherical shape of the liquid-vapor interface and a capillary wave travels along the liquid-vapor interface from the contact line to the top of the droplet. The non-uniform curvature of the droplet retards the downward contact-line motion and initiates a downward acceleration of the liquid at the top of the droplet. By roughly 10 ns, the flow initiated by these curvature deviations brings the droplet back to an *approximately* spherical shape. The liquid then moves uniformly downward in the configuration shown in Fig. 7(b) which is similar to configuration C from Fig. 1(a). During this period, the steady contact-line speed is approximately 0.1 m s^{-1} shown in Fig. 8(b), which is consistent with the estimate of viscous spreading in Table I.

By 760 ns, the liquid translates downward far enough that the liquid-vapor interface approaches the solid corner, at

29 September 2025 19:45:15

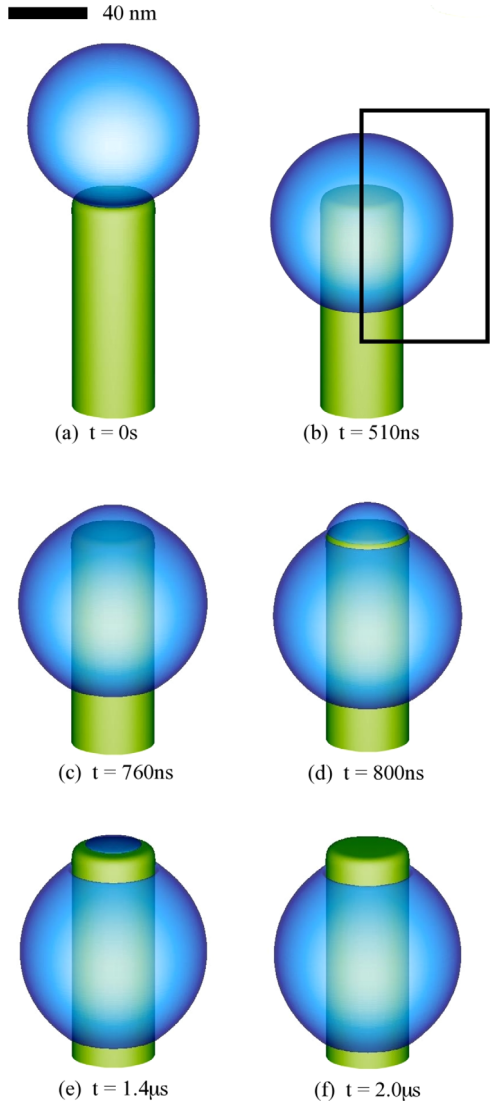

FIG. 7. (Color online) Evolution from the droplet to the annular configuration for Simulation #6. Wire radius is 22 nm. The convective flux in the boxed portion of (b) is shown in detail in Fig. 10.

which point it begins to distort, Fig. 7(c). The liquid's downward speed briefly increases, visible between (c) and (d) in Fig. 8. The liquid eventually pinches, splitting the volume into two regions. One region wets the top face and the other wets the sidewall, shown just after the splitting event in Fig. 7(d). The liquid on the top face has a larger mean curvature and is, therefore, at a higher pressure than the annular liquid volume. This results in a Gibbs-Thomson shift which causes the smaller liquid to shrink between Figs. 7(d) and 7(e), while the volume of the liquid on the sidewall increases. This increase continues to drive the lowest contact line downward, Fig. 8(e), although the velocity is roughly an order of magnitude slower than the steady spreading speed. The top of the wire is completely uncovered by 1.5 μs, at which point the contact-line speed drops toward zero, Fig. 8(f). Note that the sequence of splitting at the corner followed by the shrinking of the smaller droplet in Figs. 7(c) and 7(d) is quite similar to that observed in Figs. 5(c) and 5(d).

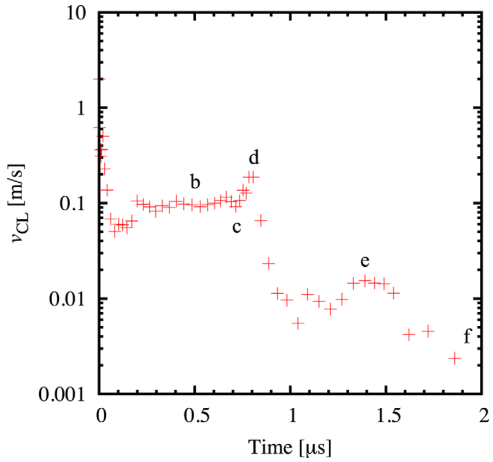

FIG. 8. (Color online) The lower contact-line speed as a function of time for a liquid undergoing a topological change from covering the top to moving to the sidewall of a nanowire. Labels b–f refer to the configurations in Figs. 7(b)–7(f), respectively.

The initial condition for this simulation is that of a spherical liquid-vapor interface with radius 40 nm, or mean curvature $h = 0.025$ nm^{-1}. During the steady spreading interval from $t = 200 - 760$ ns, the liquid-vapor interface appears spherical, but Fig. 9 shows that the mean curvature of the liquid-vapor interface is not actually spatially uniform. The plot shows h as a function of vertical distance, z, from the contact line for two different times during the steady spreading event. At both 230 and 510 ns there are gradients of curvature, with larger curvature, and therefore higher pressure, near the top of the droplet. The curvature variation leads to a pressure gradient which drives fluid flow from the top of the droplet toward the contact line, visible in Fig. 10. In addition to the instantaneous spatial variations in h, Fig. 9 shows an overall decrease in h with time. As the liquid-vapor interface moves downward, it expands to accommodate the increasing volume of solid that it wets, giving rise to the decrease in h with time. The large increase in h at the bottom of the droplet occurs within 10 nm of the contact line

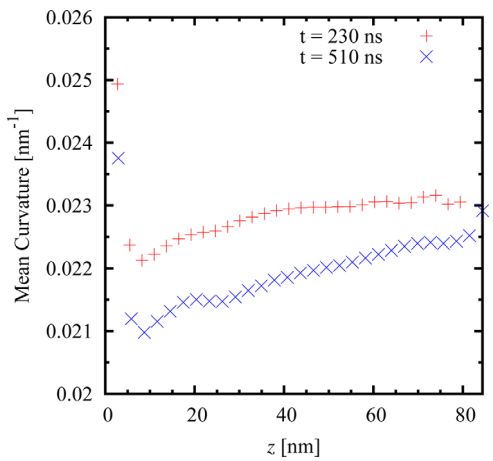

FIG. 9. (Color online) Mean curvature h of the liquid-vapor interface during steady spreading [see Fig. 7(b)] as a function of vertical distance from the contact line, z, for two different times during the steady downward spreading event. $z = 0$ corresponds to the contact line, and $z \approx 80$ nm corresponds to the top of the droplet.

29 September 2025 19:45:15

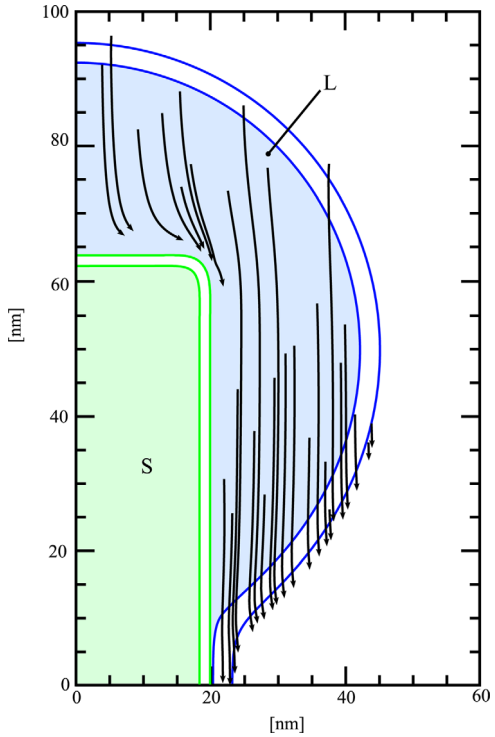

FIG. 10. (Color online) Cross section of the boxed region in Fig. 7(b) ($t = 510$ ns), with streamlines of the $\rho\vec{v}$ field. Parallel lines indicate diffuse interface regions. There is strong convective flux from the top of the droplet toward the contact line on the sidewall. This flow is driven by the curvature gradient shown in Fig. 9.

(≈ 3 interface thicknesses), and is likely an artifact of the diffuse interface model. Finally, the curvature variations visible in Fig. 9 are consistent with the estimate $\Delta R/R_0 \approx 0.05$ used in Table I.

This simulation shows that an axisymmetric transition between configurations B and D in the work of Roper *et al.*[13] is possible when the annular configuration is favored. The liquid transitions between the energy minima via configuration C as well as a second configuration with two distinct liquid volumes, shown in Figs. 7(d)–(e). This intermediate configuration is not predicted by energy minimization arguments, and is a result of the *pathway* that the droplet takes between the initial and final states. The final state with liquid wetting the sidewall is a possible route for a growth direction change.

IV. CONCLUSIONS AND FUTURE WORK

Phase-field calculations have given insights into the dynamics of contact-line motion during droplet configuration changes, and the model is in good agreement with sharp-interface theoretical predictions. The work here confirms the energy predictions made in Ref. 13, though it goes further and identifies, for the first time, the *dynamic pathways* by which topological changes occur as well as the time scales for such transitions. In addition to confirming the static, stable states of liquid droplets on nanowires, the present simulations show that transitions between states are dynamically possible. Furthermore, these simulations indicate the types of perturbations necessary to induce transitions ultimately affecting wire morphology. The volume of the liquid and the Young's angle both strongly influence the stable configuration of the droplet. A change in the growth temperature would change the liquid volume, and thus could be used to initiate a configuration change. Additionally, the Young's angle could be modified by a change in the vapor phase environment.

The configurations that have been explored both theoretically in the literature and here via numerical calculations are all axisymmetric. This symmetry is computationally convenient, but is clearly broken when nanowires kink during growth. Many nanowires are hexagonal rather than circular in cross section due to interfacial-energy anisotropy, and the faceted nature of the solid could be an important factor in the kinking process. Additionally, the top and side facets are not necessarily all of the same type, and could have different values of solid-liquid and solid-vapor surface energy. Moving forward, the addition of complex interfacial-energy anisotropy to a fully three-dimensional simulation would allow testing of droplet stability to realistic nonaxisymmetric scenarios important in kinking.

ACKNOWLEDGMENTS

The authors acknowledge helpful conversations with Dr. A.M. Anderson and Dr. S.M. Roper. This work was partially supported by NSF Grant No. CMMI-0507053, and E.J.S. acknowledges a National Defense Science and Engineering Graduate Fellowship.

[1]R. S. Wagner and W. C. Ellis, Appl. Phys. Lett. **4**, 89 (1964).
[2]R. S. Wagner and C. J. Doherty, J. Electrochem. Soc. **115**, 93 (1968).
[3]B. Tian, T. Cohen-Karni, Q. Qing, X. Duan, P. Xie, and C. M. Lieber, Science **329**, 830 (2010).
[4]M. J. Bierman and S. Jin, Energy Environ. Sci. **2**, 1050 (2009).
[5]E. J. Schwalbach, S. H. Davis, P. W. Voorhees, J. A. Warren, and D. Wheeler, J. Mater. Res. **26**, 2186 (2011).
[6]J. Westwater, D. P. Gosain, S. Tomiya, S. Usui, and H. Ruda, J. Vac. Sci. Technol., B **15**, 554 (1997).
[7]T. Kawashima, T. Mizutani, T. Nakagawa, H. Torii, T. Saitoh, K. Komori, and M. Fujii, Nano Lett. **8**, 362 (2008).
[8]A. Lugstein, M. Steinmair, Y. J. Hyun, G. Hauer, P. Pongratz, and E. Bertagnolli, Nano Lett. **8**, 2310 (2008).
[9]B. Tian, P. Xie, T. J. Kempa, D. C. Bell, and C. Lieber, Nat. Nanotechnol. **4**, 824 (2009).
[10]P. Madras, E. Dailey, and J. Drucker, Nano Lett. **10**, 1759 (2010).
[11]E. Dailey, P. Madras, and J. Drucker, J. Appl. Phys. **108**, 064320 (2010).
[12]E. Dailey, P. Madras, and J. Drucker, Appl. Phys. Lett. **97**, 143106 (2010).
[13]S. M. Roper, A. M. Anderson, S. H. Davis, and P. W. Voorhees, J. Appl. Phys. **107**, 114320 (2010).
[14]K. W. Schwarz and J. Tersoff, Phys. Rev. Lett. **102**, 206101 (2009).
[15]K. W. Schwarz and J. Tersoff, Nano Lett. **11**, 316 (2011).
[16]W. J. Boettinger, J. A. Warren, C. Beckermann, and A. Karma, Ann. Rev. Mat. Res. **32**, 163 (2002).
[17]P. Seppecher, Int. J. Eng. Sci. **34**, 977 (1996).
[18]H. Ding and P. D. M. Spelt, J. Fluid Mech. **576**, 1 (2007).
[19]W. Villanueva, K. Grönhagen, G. Amberg, and J. Ågren, Phys. Rev. E **77**, 056313 (2008).
[20]W. Villanueva, W. J. Boettinger, J. A. Warren, and G. Amberg, Acta Mater. **57**, 6022 (2009).
[21]H. Ding, M. N. H. Gilani, and P. D. M. Spelt, J. Fluid Mech. **644**, 217 (2010).
[22]D. Wheeler, J. A. Warren, and W. J. Boettinger, Phys. Rev. E **82**, 051601 (2010).
[23]S. Schiaffino and A. A. Sonin, Phys. Fluids **9**, 3172 (1997).

29 September 2025 19:45:15

[24]H. Okamoto and T. B. Massalski, Bull. Alloy Phase Diagrams **4**, 190 (1983).
[25]R. F. Sekerka and Z. Bi, *Interfaces for the 21st Century* (Imperial College Press, London, 2002), pp. 147–166.
[26]R. F. Sekerka, Philos. Mag. **91**, 3 (2011).
[27]J. E. Guyer, D. Wheeler, and J. A. Warren, Comput. Sci. Eng. **11**, 6 (2009).
[28]T. Iida and R. I. Guthrie, *The Physical Properties of Liquid Metals* (Oxford University Press, New York, 1993)
[29]J. F. Oliver, C. Huh, and S. G. Mason, J. Colloid Interface Sci. **59**, 568 (1977).

29 September 2025 19:45:15